Geometric state function for two-fluid flow in porous media

James E. McClure
Virginia Polytechnic Institute & State University, Blacksburg, Virginia, USA

Ryan T. Armstrong
University of New South Wales, Sydney, New South Wales, Australia

Mark A. Berrill
Oak Ridge National Laboratory, Oak Ridge, Tennessee, USA

Steffen Schlüter
Helmholtz-Centre for Environmental Research–UFZ, Halle (Saale), Germany

Steffen Berg
Shell Global Solutions International B.V., Amsterdam, the Netherlands

William G. Gray and Cass T. Miller
University of North Carolina at Chapel Hill, Chapel Hill, North Carolina, USA

(Received 28 July 2017; revised manuscript received 15 May 2018; published 30 August 2018)

Models that describe two-fluid flow in porous media suffer from a widely recognized problem that the constitutive relationships used to predict capillary pressure as a function of the fluid saturation are nonunique, thus requiring a hysteretic description. As an alternative to the traditional perspective, we consider a geometric description of the capillary pressure, which relates the average mean curvature, the fluid saturation, the interfacial area between fluids, and the Euler characteristic. The state equation is formulated using notions from algebraic topology and cast in terms of measures of the macroscale state. Synchrotron-based x-ray microcomputed tomography and high-resolution pore-scale simulation is applied to examine the uniqueness of the proposed relationship for six different porous media. We show that the geometric state function is able to characterize the microscopic fluid configurations that result from a wide range of simulated flow conditions in an averaged sense. The geometric state function can serve as a closure relationship within macroscale models to effectively remove hysteretic behavior attributed to the arrangement of fluids within a porous medium. This provides a critical missing component needed to enable a new generation of higher fidelity models to describe two-fluid flow in porous media.

DOI: 10.1103/PhysRevFluids.3.084306

I. INTRODUCTION

Two-phase extensions of Darcy's law were introduced on a phenomenological basis more than a half-century ago [1–4]. These models are used routinely to predict the behavior of hydrologic systems, evaluate geologic carbon sequestration, and guide the recovery of oil and gas [5–7]. A widely recognized deficiency of these models is reliance upon nonunique and history-dependent closure relationships. A prominent example is the relation used to describe the capillary pressure as a function of the fluid saturation history [8–11]. It has been hypothesized that history dependence

can be removed from the capillary pressure relation by incorporating additional state variables [10]. Despite experimental and computational efforts over the last two decades, a sufficient set of state variable has not been established to confirm this hypothesis and no general unique state equation exists to describe capillary pressure.

While models must be formulated and applied at macroscopic length scales that range from meters to kilometers, it is known that the microscopic arrangement of fluids within geologic materials has important consequences for fluid flow [12–22]. In particular, the snap-off and entrapment of fluid subregions at the pore scale has been established as an important source of hysteresis [23–26]. The impact of fluid connectivity on the system behavior has led to the development of approaches that explicitly include the portion of disconnected fluids [27–31]. Relationships that include additional state variables, such as interfacial area [25,32–37] and more recently the Euler characteristic [38–42], have also been considered.

The overall goal of this work is to develop and validate a hysteresis-free geometric state equation to describe the macroscale capillary pressure based on invariant measures. The specific objectives of this work are (1) to provide a theoretical basis for a geometric state function, (2) to produce a general functional form of the state equation in terms of macroscale measures of the state of a porous medium, (3) to define a specific state equation consistent with the general form, (4) to evaluate the state for a wide range of media and flow conditions, (5) to analyze state data in light of traditional and alternative state equations, and (6) to investigate whether the proposed state equation can describe not only equilibrium but also dynamic states of the system.

II. CAPILLARY PRESSURE

Mercury porosimetry techniques were developed to probe the geometry of a porous medium by modifying the pressure difference between two fluids, $p_c = p_n - p_w$ [43]. At equilibrium and in the absence of external forces, the pressure forces are balanced by capillary forces at points on the interface between fluids, as given in the Laplace equation:

$$p_n - p_w = \gamma_{wn}\left(\frac{1}{R_1} + \frac{1}{R_2}\right), \tag{1}$$

where R_1 and R_2 are the principal radii of curvature determined at points on the surface and γ_{wn} is the interfacial tension between fluids. Typical porous media have a range of pore sizes, and at the macroscale as the capillary pressure p^c increases the saturation of the wetting fluid, s^w, decreases [44,45]. This reasoning provides the basis for Leverett's J-function and van Genuchten's relation to predict the water retention curve in porous materials [1,2]. However, the relation $p^c(s^w)$ is material-specific and depends on the system history. A typical example of a hysteretic capillary pressure relationship is shown in Fig. 1. Different capillary pressures are observed for a given saturation depending on the flow history, meaning that a functional relationship $p^c(s^w)$ does not exist. During drainage, higher capillary pressures are needed to force the menisci through the pore throats, which are the narrowest parts of the pore space. Capillary pressures along the imbibition curve are determined by the pore body sizes, which are associated with larger radii of curvature. Snap-off and coalescence events occur frequently during displacement and alter the connectivity of the fluids. Fluid connectivity is recognized as an important component of the system state, and key features of the capillary pressure relationship correspond with the limits where fluid connectivity breaks down. The residual nonwetting phase saturation corresponds to a situation where the nonwetting fluid is completely disconnected and ceases to transmit a pressure gradient across a system. Similarly, the irreducible wetting phase saturation is reached when wetting phase connectivity breaks down. These values are often used as parameters in empirical functional forms used to fit experimental data for capillary pressure and relative permeability to account for the role of fluid connectivity [2–4].

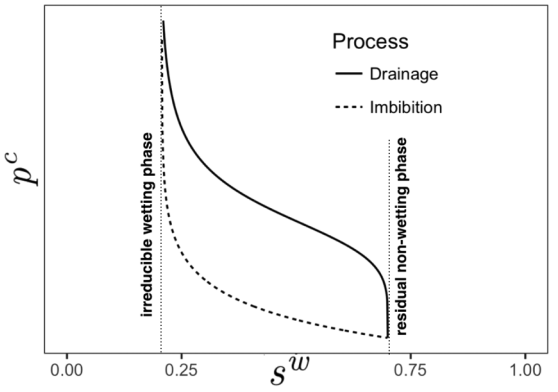

FIG. 1. The shape of drainage and imbibition curves are determined in part by the fluid connectivity. The irreducible wetting phase and residual nonwetting phase saturations correspond to limits where fluid connectivity breaks down.

III. GEOMETRIC STATE MEASURES

Invariant geometric quantities provide a natural mechanism to characterize the complex arrangements of fluid and solid phases within porous media [46–50]. The mathematical underpinnings for this approach are provided by Hadwiger's theorem, which demonstrates that only four averaged measures, the Minkowski functionals (MFs), are needed to characterize the morphology of a three-dimensional object [51–54]. We consider the nonwetting phase domain, $\Omega_n \in \Omega$, with boundary Γ_n, where Ω is the domain occupied by a porous medium. The MFs can be considered as macroscale invariants that are obtained directly from microscale invariants using integral geometry. The first pair of MFs are the volume and the surface area:

$$M_0^n = \lambda(\Omega_n) = \int_{\Omega_n} dr, \tag{2}$$

$$M_1^n = \lambda(\Gamma_n) = \int_{\Gamma_n} dr, \tag{3}$$

where λ denotes the Lebesgue measure. The second pair of MFs are averages of the two microscale surface invariants on Γ_n; these are the mean curvature and the Gaussian curvature. The associated MFs are

$$M_2^n = \int_{\Gamma_n} \left(\frac{1}{R_1} + \frac{1}{R_2} \right) dr \quad \text{and} \tag{4}$$

$$M_3^n = \int_{\Gamma_n} \frac{1}{R_1 R_2} dr. \tag{5}$$

Each of the MFs measures the size of Ω_n in various dimensions: volume (ℓ^3), surface area (ℓ^2), integral mean curvature (ℓ), and the Euler characteristic

$$\chi^n = \frac{M_3^n}{4\pi}. \tag{6}$$

The Euler characteristic relates to the total curvature by the Gauss-Bonnet theorem, and serves as an average measure for the connectivity of the fluid based on the possible channels and disconnected regions [48,55,56]. Topological theory links the Euler characteristic to the number of connected

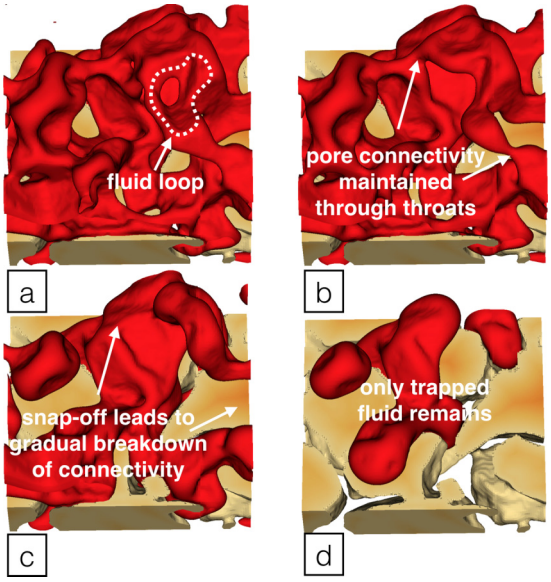

FIG. 2. Sequence showing the pore-level evolution of the nonwetting fluid geometry during imbibition of the wetting fluid. As the volume fraction of the nonwetting fluid volume decreases, corresponding changes in the surface area, mean curvature, and connectivity also occur.

components B_0^n, loops B_1^n, and cavities B_2^n:

$$\chi^n = B_0^n - B_1^n + B_2^n. \tag{7}$$

The quantities B_0^n, B_1^n, and B_2^n are topological invariants known as the Betti numbers. The pore-level view illustrated in Fig. 2 provides insight into the relationship between the Betti numbers and the nonwetting fluid connectivity. In this case, the volume fraction of the nonwetting fluid is decreasing from Fig. 2(a)–2(d) due to imbibition of the wetting fluid. The geometric evolution of the nonwetting fluid occurs based on incremental changes to the volume, surface area, curvature and connectivity. These changes are coupled. In the well-connected system shown in Fig. 2(a), redundant connectivity is evident based on the presence of loops. As the fluid volume fraction decreases, connections made through the pore throats are broken due to snap off, eventually leaving only nonwetting fluid components that are disconnected from each other in Fig. 2(d). The Euler characteristic quantifies these effects.

The basis for characterization of the nonwetting fluid is provided by a generalized form of Steiner's formula that applies for sets with positive reach [55]

$$\lambda(\Omega_n \oplus \varsigma_\delta) - \lambda(\Omega_n) = \sum_{i=1}^{3} a_i M_i^n \delta^i, \tag{8}$$

where ς_δ is a spherical ball with radius δ and $\oplus$ denotes the Minkowski sum. Steiner's formula predicts the volume of the parallel set $\Omega_n \oplus \varsigma_\delta$ for a particular geometric configuration. The coefficients a_i are determined by the shape of Ω_n. Equation (8) shows that sufficiently small changes in the volume of Ω_n are locally smooth and continuous functions of the MFs [51,55]. The assumption that Ω_n has positive reach means that for some positive δ the ball ς_δ could be rolled around the boundary without intersecting Ω_n. The nonwetting fluid will in general meet this criterion. As an illustrative example, consider the two-dimensional object shown in Fig. 3. In this case, the blue region is produced by rolling a small ball around the boundary of the red object (i.e., Ω_n). The area of the blue region is determined only by the properties of the red region boundary and the size of the ball. This is the

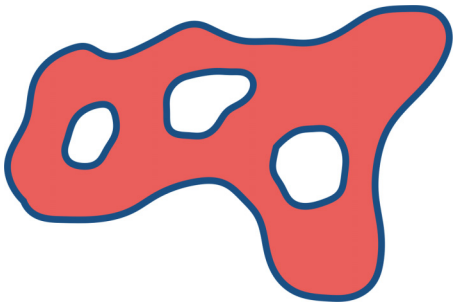

FIG. 3. Two-dimensional analog for Eq. (9): the change in area (blue region) obtained by rolling a small ball around the boundary for a 2D object (red region) is determined by the shape of the red object boundary and can be expressed in terms of averaged measures of the boundary shape.

meaning of Eq. (8). The red object has positive reach because the blue region does not overlap with the red object at any point along the boundary. However, the red object is not a convex set; if a large enough ball were rolled along the boundary, the holes in the middle of the object would be closed by the operation $\Omega_n \oplus \varsigma_\delta$. This would irrevocably alter the topology of the object. For this reason Eq. (8) will hold only if the ball ς_δ is sufficiently small. When the boundary of the wetting and solid phases include grain contacts, the associated sets will not have positive reach. This motivates our choice to characterize the nonwetting fluid.

Since the MFs are extensive properties, it is useful to divide Eq. (8) by the total volume,

$$\Delta\epsilon^n = \frac{\lambda(\Omega_n \oplus \varsigma_\delta) - \lambda(\Omega_n)}{V} = \sum_{i=1}^{3} \frac{a_i M_i^n \delta^i}{V}, \tag{9}$$

where $\Delta\epsilon^n$ is the change in the nonwetting phase volume fraction that results from the operation $\Omega_n \oplus \varsigma_\delta$. Equation (9) is a kinematic statement that holds locally; the volume of an object changes only as a consequence of net movement of the object boundary. The associated change in volume can be expressed in terms of the invariant properties of the boundary: surface area, integral mean curvature, and total curvature. Based on these arguments, Eq. (9) provides a geometric relationship to predict the change in volume for a particular object.

From the standpoint of model development, it is further necessary to connect geometry to thermodynamics so that processes involving energy dissipation can be described. The thermodynamically constrained averaging theory (TCAT) provides a framework to accomplish this objective. TCAT models are developed by applying rigorous averaging procedures to directly connect microscale thermodynamics and continuum mechanical forms with their macroscale counterparts [57–59]. Within TCAT, capillary pressure is the product of the average mean curvature of the interface between fluids, J_w^{wn}, and the interfacial tension between the two fluids. Relevant geometric measures are listed in Table I. Based on these measures, a clear connection to thermodynamics is established:

TABLE I. Relevant geometric measures included in TCAT.

Quantity	Description
ϵ	Porosity
ϵ^n	Volume fraction of the nonwetting fluid
ϵ^{wn}	Surface area per unit volume for the wn interface
ϵ^{ns}	Surface area per unit volume for the ns interface
J_w^{wn}	Average mean curvature of wn interface
J_s^{ns}	Average mean curvature of ns interface

phase volume fractions and specific interfacial areas are needed to predict the internal energy of the macroscopic system using appropriate thermodynamic expressions. The possible values for these quantities are constrained by geometric laws.

The first three Minkowski functionals can be expressed directly in terms of the quantities listed in Table I,

$$M_0^n = \epsilon^n V, \tag{10}$$

$$M_1^n = (\epsilon^{wn} + \epsilon^{ns})V, \tag{11}$$

$$M_2^n = \left(J_w^{wn}\epsilon^{wn} + J_s^{ns}\epsilon^{ns}\right)V, \tag{12}$$

where V is the volume of Ω. A nondimensional form is obtained by introducing the Sauter mean diameter as a reference length scale, $D = 6\epsilon/(\epsilon^{ns} + \epsilon^{ws})$, and defining $\acute{\delta} \equiv \delta/D$. In terms of these alternate quantities, Eq. (9) becomes

$$\Delta\epsilon^n = a_1(\acute{\epsilon}^{wn} + \epsilon^{ns}D)\acute{\delta} + a_2\left(\acute{J}_w^{wn}\acute{\epsilon}^{wn} + J_s^{ns}\epsilon^{ns}D^2\right)\acute{\delta}^2 + a_3\acute{\chi}^n\acute{\delta}^3. \tag{13}$$

Three nondimensional quantities have been introduced:

$$\acute{\epsilon}^{wn} = \epsilon^{wn}D, \tag{14}$$

$$\acute{J}_w^{wn} = J_w^{wn}D, \text{ and} \tag{15}$$

$$\acute{\chi}^n = \chi^n D^3/V. \tag{16}$$

Based on Eq. (13), different objects will yield different coefficients a_i according to Minkowski's quermassintegral [51]. For example, it is not obvious that two different objects with identical Minkowski functionals would also have the same coefficients. Thus it remains to be demonstrated that Eq. (9) will produce unique relationships between the Minkowski functionals that will hold for two-fluid flow. In this work this postulate is tested computationally by considering a very large number of geometric states. We consider the case where the porosity ϵ is constant and the role of the fluid volumes is included from the saturation, $s^w = \epsilon^w/\epsilon = (1 - \epsilon^n)/\epsilon$. We further assume that $J_s^{ns}(s^w, \acute{\epsilon}^{wn}, \acute{\chi}^n)$ and $\epsilon^{ns}(s^w, \acute{\epsilon}^{wn}, \acute{\chi}^n)$. We therefore pose the geometric state function as $\acute{J}_w^{wn}(s^w, \acute{\epsilon}^{wn}, \acute{\chi}^n)$. This form reflects the fact that the solid is immobile and movement of the nonwetting phase boundary occurs only at the interface between the two fluids. Numerical results used in conjunction with experimental data will be used to show that this relationship is able to characterize the possible nonwetting fluid configurations in porous media.

IV. INK BOTTLE EXAMPLE

Ink bottles such as the example shown in Fig. 4 are often used to illustrate the reason for history dependence in the capillary pressure relation. The ink bottle geometry is a surface of revolution of a piecewise smooth function $\rho(x) > 0$, which determines the width of the channel as a function of position x. The ink bottle shown in Fig. 4(a) is produced by considering five equally sized circles with radius R, positioned to create a sequence of pore bodies connected by throats of various sizes. The minimum width for each of the three throats is H_1, H_2, and H_3, respectively. For the case at hand we choose $R = 1.0$ mm, $H_1 = 0.6$ mm, $H_2 = 0.4$ mm, and $H_3 = 0.2$ mm. The $\{x, y\}$ coordinates for the circle centers are given by

$$\boldsymbol{c}^{(1)} = \{R, H_1 + R\}, \tag{17}$$

$$\boldsymbol{c}^{(2)} = \left\{c_x^{(1)} + \sqrt{4R^2 - (H_1 + R)^2}, 0\right\}, \tag{18}$$

$$\boldsymbol{c}^{(3)} = \left\{c_x^{(2)} + \sqrt{4R^2 - (H_2 + R)^2}, H_2 + R\right\}, \tag{19}$$

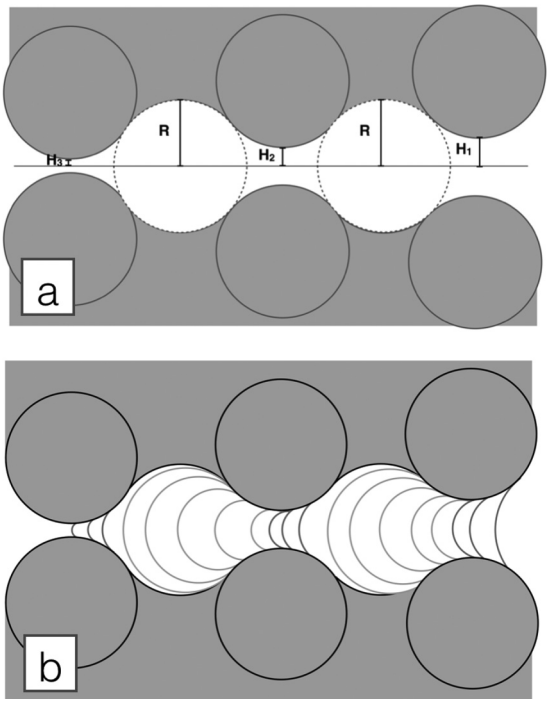

FIG. 4. (a) The ink bottle geometry is defined based on the position of five equally sized spheres in a symmetric system with radius R to create a two-pore system connected to three throats with widths H_1, H_2, and H_3. (b) Meniscus configurations within the ink bottle can be determined analytically.

$$\boldsymbol{c}^{(4)} = \left\{c_x^{(3)} + \sqrt{4R^2 - (H_2 + R)^2}, 0\right\}, \tag{20}$$

$$\boldsymbol{c}^{(5)} = \left\{c_x^{(4)} + \sqrt{4R^2 - (H_3 + R)^2}, H_3 + R\right\}. \tag{21}$$

The position of the ink bottle wall is given by $\rho(x)$, which is determined based on the five circles,

$$\rho(x) = \begin{cases} c_y^{(1)} + R\sin\left(\arccos\frac{x-c_x^{(1)}}{R}\right) & \text{for } x < x_1 \\ -R\sin\left(\arccos\frac{x-c_x^{(2)}}{R}\right) & \text{for } x_1 \leqslant x < x_2 \\ c_y^{(3)} + R\sin\left(\arccos\frac{x-c_x^{(3)}}{R}\right) & \text{for } x_2 \leqslant x < x_3 \\ -R\sin\left(\arccos\frac{x-c_x^{(4)}}{R}\right) & \text{for } x_3 \leqslant x < x_4 \\ c_y^{(5)} + R\sin\left(\arccos\frac{x-c_x^{(5)}}{R}\right) & \text{for } x_4 \leqslant x \end{cases}, \tag{22}$$

where the contact points between the circles are

$$x^{(1)} = c_x^{(1)} + \sqrt{R^2 - (H_1 + R)^2/2}, \tag{23}$$

$$x^{(2)} = c_x^{(2)} + \sqrt{R^2 - (H_2 + R)^2/2}, \tag{24}$$

$$x^{(3)} = c_x^{(3)} + \sqrt{R^2 - (H_2 + R)^2/2}, \tag{25}$$

$$x^{(4)} = c_x^{(4)} + \sqrt{R^2 - (H_3 + R)^2/2}. \tag{26}$$

From the standpoint of an experiment, there are two basic ways to impact the geometric state within a porous medium. First, one can can inject fluid into the system from the boundary, explicitly

controlling the volume of fluid injected and allowing the fluid pressures to adjust. Second, one can control the pressure for each fluid at the boundary, allowing the fluid volumes to adjust until a stable equilibrium is achieved. Any sensible description of the system must be able to describe either scenario. We consider the quasistatic case for which the difference in fluid pressures is exactly balanced by the capillary pressure based on the Laplace equation. The fluid pressures are constant within their respective phase regions and the curvature is constant over the meniscus (i.e., $p^c = -\gamma^{wn} J_w^{wn}$). The macroscale fluid-fluid interfacial tension is constant and the contact angle is zero degrees.

Fluid displacement within the ink bottle proceeds with the nonwetting fluid invading from the right boundary of Fig. 4 as the difference between the fluid pressure increases, and the wetting fluid exiting at the left. Geometric measures for the nonwetting fluid are determined based on the position of the contact line in the x direction. Meniscus configurations can be determined based on $\rho(x)$ and its derivative. When the common curve is at x, the meniscus curvature is

$$r(x) = \rho\sqrt{1 + \left(\frac{d\rho}{dx}\right)^2}. \tag{27}$$

The height of the spherical cap is

$$h(x) = r - \rho\left(\frac{d\rho}{dx}\right). \tag{28}$$

Note that for the quasistatic displacements shown in Fig. 4(b) the position of the common curve will always be within a pore throat. The nonwetting fluid volume fraction, interfacial areas per unit volume, and mean curvature for each interface are each determined by the position of the common curve,

$$\epsilon^n(x) = \frac{\pi}{V}\left[\int_0^x \rho^2\, dx' + \frac{1}{6}h(3\rho^2 + h^2)\right], \tag{29}$$

$$\epsilon^{wn}(x) = \frac{2\pi r h}{V}, \tag{30}$$

$$J_w^{wn}(x) = \frac{2}{r}, \tag{31}$$

$$\epsilon^{ns}(x) = \frac{2\pi}{V}\int_0^x \rho\sqrt{1 + \left(\frac{d\rho}{dx'}\right)^2}\, dx', \tag{32}$$

$$J_s^{ns}(x) = \frac{2\pi}{\epsilon^{ns} V}\int_0^x \rho\left(\frac{1}{r_1} + \frac{1}{r_2}\right)\sqrt{1 + \left(\frac{d\rho}{dx'}\right)^2}\, dx', \tag{33}$$

where $r_1(x)$ and $r_2(x)$ are the two principal radii of curvature for the ink bottle wall. Since the geometry is a surface of revolution, $r_1 = \rho$. Within the pores $r_2 = R$. Within the throats $r_2 = -R$. Quasistatic displacements within the ink bottle can be described analytically based on these expressions.

As p_c increases, the meniscus squeezes through the pore throats leading to a decrease in s^w. Pore filling occurs spontaneously during drainage based on the sequence of blue menisci in Fig. 4(b). The red and blue menisci are associated with the red and blue portions of the curve in Figs. 5(a) and 5(b), respectively. Based on Fig. 5(a) the equilibrium meniscus curvature is apparently lower during imbibition as compared to drainage. However, the fluid volume can change only due to movement of the meniscus and changes in the geometric state are kinematic in nature. While traditionally $p^c(s^w)$ considers only stable equilibrium menisci (red), under quasistatic conditions the same configurations are obtained independent from flow direction, which includes blue portions of the curve in Figs. 5(a) and 5(b). The apparent hysteresis is removed when the geometric trajectory of the system is considered.

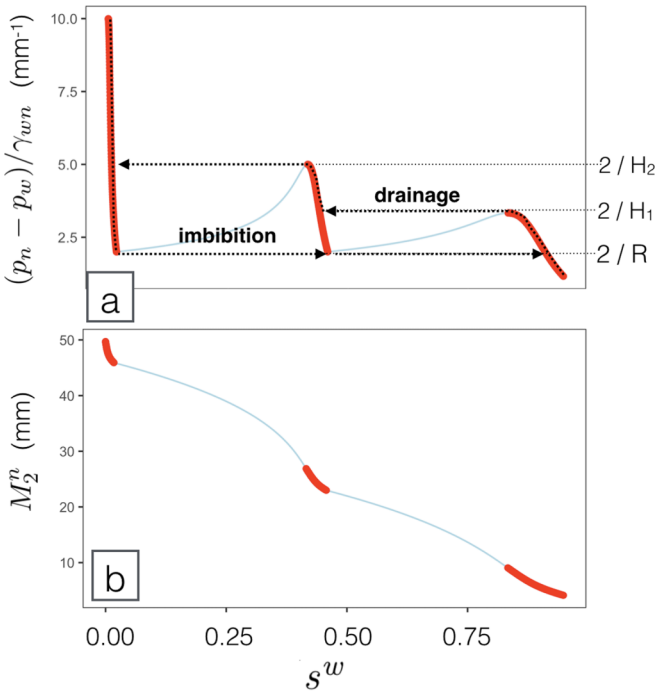

FIG. 5. (a) Apparent hysteresis in the ink bottle results from the observation of apparently different equilibrium states for drainage and imbibition; (b) the integral mean curvature is a one-to-one function of the saturation.

To see more clearly how the Minkowski functionals remove the apparent hysteresis in the ink bottle, we consider the integral mean curvature

$$M_2^n = \left(J_w^{wn}\epsilon^{wn} + J_s^{ns}\epsilon^{ns}\right)V. \tag{34}$$

Figure 5(b) shows that there is a one-to-one relationship between M_2^n and s^w. While the curvature J_w^{wn} is not a one-to-one function of s^w, it can be clearly inferred based on M_2^n, ϵ^{wn}, ϵ^{ns}, and the curvature of the solid J_s^{ns}. Since all quantities in Eqs. (29)–(33) are functions of x, only a single degree of freedom exists for the ink bottle problem; each quantity is uniquely determined by the position of the common curve. It is also important to note that for the ink bottle geometry the integral mean curvature and surface area are not independent quantities since the ink bottle is a surface of revolution. Ink bottles are generated by rotating two-dimensional objects with fewer geometric degrees of freedom; radial symmetry leads to menisci that are perfect spherical caps. For a spherical meniscus, the surface area is directly determined by the curvature. This contrasts with real porous media where the surface area and mean curvature are independent quantities. Furthermore, the ink bottle provides only a single channel for flow such that complex fluid connectivity is impossible (i.e., $\chi^n = 1$). This is an important reason why fewer geometric invariants are needed to characterize states within the ink bottle. It is therefore essential to consider more complex geometries to understand the possible geometric states within porous media.

V. POROUS MEDIA AND FLOW CONDITIONS

The microscopic details of fluid and solid materials can be observed experimentally from microcomputed tomography (μCT) [39,60–62]. The resulting data can be used to measure interfacial curvatures, surface areas, the Euler characteristic, and phase connectivity. Six different solid materials and relevant properties are listed in Table II. These include one synthetic sphere pack and five

TABLE II. Summary of rock geometries and simulation conditions considered in this work.

Media	ϵ	D (mm)	Size (voxels)	Sim.	Config.
Castlegate	0.205	0.111	$512 \times 512 \times 512$	A, D	23 123
Estaillades	0.111	0.124	$834 \times 834 \times 556$	A, B, D	23 599
Gildehauser	0.188	0.133	$852 \times 852 \times 569$	A, B, D	38 788
Robuglass	0.345	0.173	$988 \times 988 \times 598$	A, B, D	49 515
Sand pack	0.376	0.368	$512 \times 512 \times 512$	A, C, D	64 650
Sphere pack	0.369	1.00	$900 \times 900 \times 900$	A, C, D	59 341

different μCT images: robuglass, sandpack, carbonate rock (Estaillades), and two sandstones (Gildehauser and Castlegate). The robuglass, Gildehauser and Estaillades data sets were processed using gradient-based segmentation, which is known to provide a valid representation of the resolved rock geometry [63]. The remaining three data sets are associated with previously published work and are publicly accessible [64,65].

For each geometry, we rely on direct numerical simulation within the observed rock geometries to generate a large number of states as needed to evaluate $\acute{J}_w^{wn}(s^w, \acute{\epsilon}^{wn}, \acute{\chi}^n)$ [66]. On the basis of pore-level occupancy and connectivity, close agreement was previously demonstrated between simulated geometries and those observed from experiment using fast μCT [39]. Since different physical processes produce different fluid arrangements, multiple simulation conditions were considered, including (a) equilibrium simulations with a random initial condition [41], (b) steady-state flow with an initial condition from μCT experiment [39], (c) steady-state flow with an initial condition from morphological opening [38,67–69], and (d) displacement with changing saturation driven by pressure boundary conditions. The initial conditions and simulation types are listed in Table II, along with the total number of distinct fluid configurations generated. Additional descriptions of the simulations are provided in the Supplemental Materials along with the geometric data generated for each material [70].

VI. MACROSCALE CLOSURE RELATIONS

For each porous medium three constitutive relationships were evaluated: $\acute{J}_w^{wn}(s^w)$, $\acute{J}_w^{wn}(s^w, \acute{\epsilon}^{wn})$, and $\acute{J}_w^{wn}(s^w, \acute{\epsilon}^{wn}, \acute{\chi}^n)$. To adequately assess the uniqueness of a relationship with three possible degrees of freedom, a large number of states must be considered. The present study includes a total of 259 016 fluid configurations for six different porous media. Averaged measures were determined from simulated microstates using an *in situ* analysis framework [71,72]. The measured values of $\acute{J}_w^{wn}$, s^w, $\acute{\epsilon}^{wn}$, and $\acute{\chi}^n$ are shown in Figs. 6(a)–6(f). Generalized additive models (GAMs) were used to construct locally smooth spline surfaces to approximate each of the three possible state functions based on the data shown in Fig. 6. The GAMs were used to approximate each relationship, evaluate the error, and to make comparisons among the three approximations [41,73]. The GAM can be considered as a numerical approach to evaluate the coefficients in Eq. (8) and determine if the relationship is unique for all microstates.

The nonuniqueness of $\acute{J}_w^{wn}(s^w)$ and $\acute{J}_w^{wn}(s^w, \acute{\epsilon}^{wn})$ can be assessed visually based on Fig. 7. A collection of curves are generated by simulating imbibition based on a set of initial conditions determined based on morphological drainage. In each case, the meniscus curvature decreases during the imbibition process, but distinctly different geometric states are obtained along each trajectory. The relationship $\acute{J}_w^{wn}(s^w)$ is clearly nonunique since multiple values of $\acute{J}_w^{wn}$ are observed at constant s^w. Furthermore, from Fig. 7(b) we see that $\acute{J}_w^{wn}(s^w, \acute{\epsilon}^{wn})$ is also nonunique; for a set of states with $s^w = 0.65$ [one for each curve in Fig. 7(a)] we see that the different $\acute{J}_w^{wn}$ may be observed for the same values of both s^w and $\acute{\epsilon}^{wn}$. Examining the Euler characteristic demonstrates that different fluid connectivity is observed within this set of states, suggesting the underlying reason for the behavior. This also illustrates the importance of generating redundant geometric states to test the uniqueness

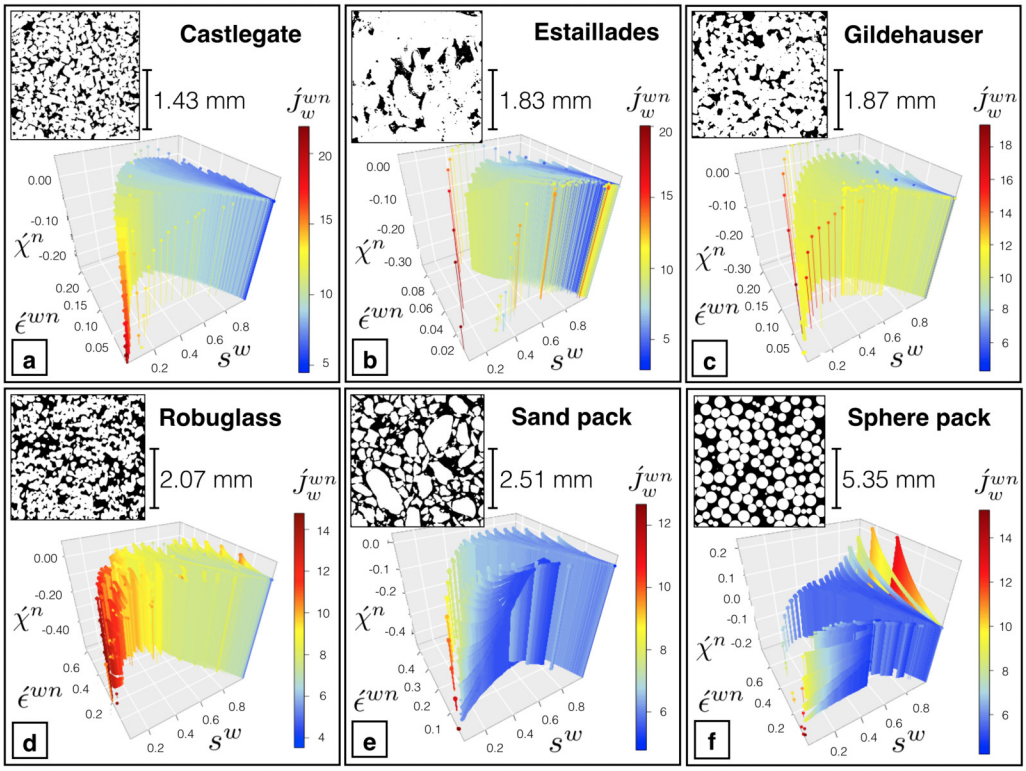

FIG. 6. The relationship between geometric state variables is explored based on the possible fluid microstates in six porous media, each with a distinct solid microstructure (white).

of the geometric relationship. A limiting factor in previous studies is that an insufficient number of points were generated for a particular volume fraction.

In Fig. 8 two different error measures are used to assess each model. Generalized cross validation (GCV) considers how accurately each data point is predicted by all remaining data points [74].

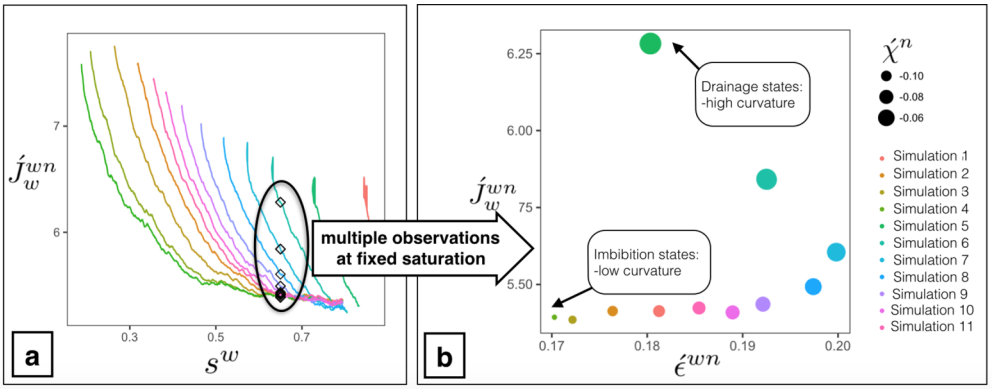

FIG. 7. Traditional models assume that the macroscale capillary pressure is a function only of the saturation of the wetting fluid. Two-fluid displacement simulations within a sand pack show that: (a) At fixed saturation, s^w, the relative mean curvature $\acute{J}_w^{wn}$ can attain many possible values depending on the system history; (b) $\acute{J}_w^{wn}(s^w, \acute{\epsilon}^{wn})$ is nonunique for $s^w = 0.65$.

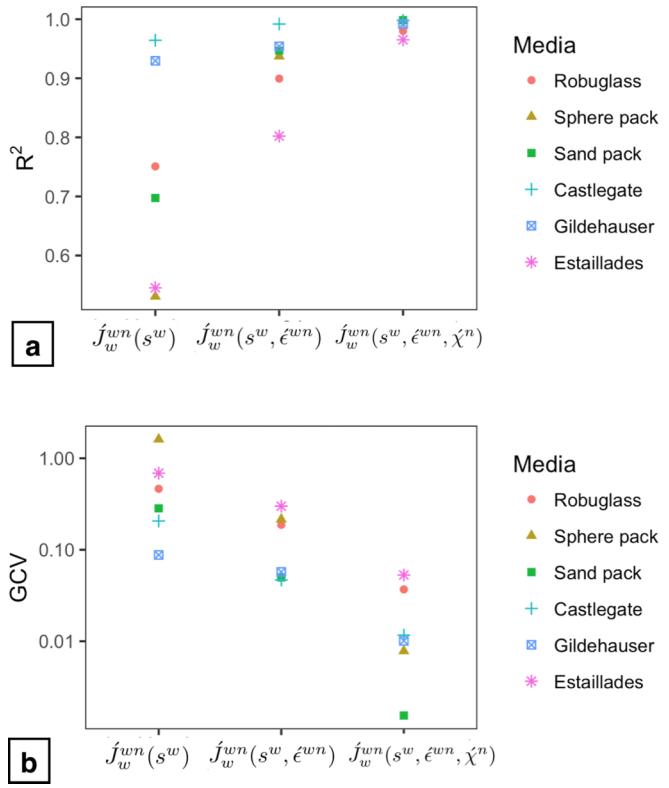

FIG. 8. The geometric state function $\acute{J}_w^{wn}(s^w, \acute{\epsilon}^{wn}, \acute{\chi}^n)$ is unique for each geometry, which is not the case for $\acute{J}_w^{wn}(s^w)$ and $\acute{J}_w^{wn}(s^w, \acute{\epsilon}^{wn})$. Locally smooth approximations were generated for each relationship using generalized additive models (GAMs) to compare the accuracy of macroscopic constitutive models. Error measures are given by (a) the coefficient of variation R^2 and (b) generalized cross validation (GCV).

The GCV will be 0.0 if the surface perfectly predicts the data. A second measure is the coefficient of determination, R^2, which measures the fraction of the variance in the underlying data points predicted based on the GAM. The value of R^2 will be 1.0 for a unique surface. The fact that $\acute{J}_w^{wn}(s^w)$ is not unique for any of the six materials is confirmed by the large GCV ($0.0878 \leqslant \text{GCV} \leqslant 1.613$) and a relatively small R^2 ($0.53 \leqslant R^2 \leqslant 0.96$). The sphere pack, sand pack, and carbonate allow for the widest range of possible fluid configurations at any given saturation, and show the largest unexplained variance for $\acute{J}_w^{wn}(s^w)$. The two sandstones and robuglass samples show the least variance. Traditionally the unexplained variance would be attributed to hysteresis. In all cases, the unexplained variance is reduced by including the interfacial area, $\acute{J}_w^{wn}(s^w, \acute{\epsilon}^{wn})$, with $0.057 \leqslant \text{GCV} \leqslant 0.30$ and $0.80 \leqslant R^2 \leqslant 0.99$. When all three independent MFs are included, $\acute{J}_w^{wn}(s^w, \acute{\epsilon}^{wn}, \acute{\chi}^n)$, the accuracy improves dramatically with $0.0015 \leqslant \text{GCV} \leqslant 0.053$ and $0.96 \leqslant R^2 \leqslant 1.0$. The only material for which $\acute{J}_w^{wn}(s^w, \acute{\epsilon}^{wn}, \acute{\chi}^n)$ captures less than 99% of the variance in the underlying data is the carbonate, shown in Fig. 6(b). Since $\acute{J}_w^{wn}(s^w, \acute{\epsilon}^{wn})$ explains only 80% of the variance for fluid configurations within the carbonate, this is also the material for which adding the Euler characteristic provides the most significant improvement. The implication is that a significant fraction of the variance in the carbonate is due to changes in fluid connectivity that are not predicted by changes in interfacial area.

In all six cases, $\acute{J}_w^{wn}(s^w)$ is observed to be nonunique. While this is mitigated when using $\acute{J}_w^{wn}(s^w, \acute{\epsilon}^{wn})$, the Euler characteristic must be included to obtain a unique relationship. Non-uniqueness in $\acute{J}_w^{wn}(s^w, \acute{\epsilon}^{wn}, \acute{\chi}^n)$ is observed only when $s^w \to 1$. This occurs because the quantities $\acute{\epsilon}^{wn}, \acute{\chi}^n$ approach zero in the limit of vanishing saturation, whereas no limit exists for

$\acute{J}_w^{wn}$ [41]. Numerical errors associated with the measurement of the interfacial area, curvature, and Euler characteristic are expected to account for a contribution to the error. Since the experimental and simulated nonwetting fluid configuration make use of a closed three-dimensional object, errors due to system size do not undermine the effort to test the validity of $\acute{J}_w^{wn}(s^w, \acute{\epsilon}^{wn}, \acute{\chi}^n)$.

The notion of a representative elementary volume (REV) is important to produce generalizable geometric state information based on microscopic measurements. In this work, we have shown that the form $\acute{J}_w^{wn}(s^w, \acute{\epsilon}^{wn}, \acute{\chi}^n)$ is valid based on nonwetting fluid configurations in water-wet porous media based on state-of-the-art μCT data. While the physical size of the systems considered in this work remains relatively small, future advancement of μCT and computing technologies will lead to growth in 3D image sizes that will continue for the foreseeable future. Based on this trajectory, REV-scale observations of porous medium microstructure are likely. These trends favor the development new models that are able to leverage the additional geometric information that is now available for flow in porous media. While factors such as length-scale heterogeneity will remain an important consideration for flow in porous media (i.e., characterization of geologic reservoirs), macroscopic strategies to address this problem are already under active development.

VII. CONCLUSIONS

We present a geometric state function to predict the mean curvature of the interface between fluids in porous medium based on a relationship between invariants established by integral geometry. The relationship accurately captures a broad range of possible fluid configurations, and can be combined with modern averaging methods to formulate a class of model that evolves interfacial areas using conservation equations and kinematic equations, applies to all water saturation levels, and does not require equilibrium assumptions [58,59,75]. To take full advantage of the equation of state developed, an evolution equation for the Euler characteristic would be needed. It is expected that this development and the proven need for this remaining quantity will catalyze efforts to develop the missing kinematic relation for the Euler characteristic. The geometric result suggests that it is possible to overcome shortcomings associated with empirical and history-dependent constitutive relationships for two-fluid flow in porous media.

ACKNOWLEDGMENTS

This work was supported by Army Research Office Grant No. W911NF-14-1-02877 and National Science Foundation Grant No. 1619767. We acknowledge the Paul Scherrer Institut, Villigen, Switzerland, for provision of synchrotron radiation beamtime at beamline TOMCAT of the SLS and would like to thank Kevin Mader and Federica Marone for assistance, and Shell for giving access to the data and supporting publication of this work. An award of computer time was provided by the Department of Energy INCITE program. This research also used resources of the Oak Ridge Leadership Computing Facility, which is a DOE Office of Science User Facility supported under Contract No. DE-AC05-00OR22725. This manuscript has been authored by UT-Battelle, LLC under Contract No. DE-AC05-00OR22725 with the US Department of Energy. The United States Government retains and the publisher, by accepting the article for publication, acknowledges that the United States Government retains a nonexclusive, paid-up, irrevocable, worldwide license to publish or reproduce the published form of this manuscript, or allow others to do so, for United States Government purposes. The Department of Energy will provide public access to these results of federally sponsored research in accordance with the DOE Public Access Plan (http://energy.gov/downloads/doe-public-access-plan).

[1] M. C. Leverett, Capillary behavior in porous solids, Petroleum Transactions, AIME **142**, 152 (1941).

[2] M. T. van Genuchten, A closed-form equation for predicting the hydraulic conductivity of unsaturated soils, Soil Sci. Soc. Am. J. **44**, 892 (1980).

[3] R. H. Brooks and A. T. Corey, Properties of porous media affecting fluid flow, J. Irrig. Drain. Div., Proc. Am. Soc. Civ. Eng. **92**, 61 (1966).
[4] Y. Mualem, Hysteretical models for prediction of the hydraulic conductivity of unsaturated porous media, Water Resour. Res. **12**, 1248 (1976).
[5] R. Juanes, E. J. Spiteri, F. M. Orr, and M. J. Blunt, Impact of relative permeability hysteresis on geological CO_2 storage, Water Resour. Res. **42**, W12418 (2006).
[6] M. L. Szulczewski, C. W. MacMinn, H. J. Herzog, and R. Juanes, Lifetime of carbon capture and storage as a climate-change mitigation technology, Proc. Natl. Acad. Sci. USA **109**, 5185 (2013).
[7] S. Berg, S. Oedai, A. J. Landman, N. Brussee, M. Boele, R. Valdez, and K. van Gelder, Miscible displacement of oils by carbon disulfide in porous media: Experiments and analysis, Phys. Fluids **22**, 113102 (2010).
[8] B. Amaziane, J. P. Milisic, M. Panfilov, and L. Pankratov, Generalized nonequilibrium capillary relations for two-phase flow through heterogeneous media, Phys. Rev. E **85**, 016304 (2012).
[9] J. Bear, B. Rubinstein, and L. Fel, Capillary pressure curve for liquid menisci in a cubic assembly of spherical particles below irreducible saturation, Transp. Porous Media **89**, 63 (2011).
[10] S. M. Hassanizadeh and W. G. Gray, Toward an improved description of the physics of two-phase flow, Adv. Water Res. **16**, 53 (1993).
[11] J. E. Killough, Reservoir simulation with history-dependent saturation functions, SPEJ **16**, 37 (1976).
[12] M. Ferer, G. S. Bromhal, and D. H. Smith, Two-phase flow in porous media: Crossover from capillary fingering to compact invasion for drainage, Phys. Rev. E **71**, 026303 (2005).
[13] D. Reeves and D. H. Rothman, Impact of structured heterogeneities on reactive two-phase porous flow, Phys. Rev. E **86**, 031120 (2012).
[14] R. Holtzman and E. Segre, Wettability Stabilizes Fluid Invasion into Porous Media via Nonlocal, Cooperative Pore Filling, Phys. Rev. Lett. **115**, 164501 (2015).
[15] R. Hilfer, R. T. Armstrong, S. Berg, A. Georgiadis, and H. Ott, Capillary saturation and desaturation, Phys. Rev. E **92**, 063023 (2015).
[16] K. T. Tallakstad, H. A. Knudsen, T. Ramstad, G. Lovoll, K. J. Maloy, R. Toussaint, and E. G. Flekkoy, Steady-State Two-Phase Flow in Porous Media: Statistics and Transport Properties, Phys. Rev. Lett. **102**, 074502 (2009).
[17] L. Cueto-Felgueroso and R. Juanes, Nonlocal Interface Dynamics and Pattern Formation in Gravity-Driven Unsaturated Flow through Porous Media, Phys. Rev. Lett. **101**, 244504 (2008).
[18] C. U. Hatiboglu and T. Babadagli, Pore-scale studies of spontaneous imbibition into oil-saturated porous media, Phys. Rev. E **77**, 066311 (2008).
[19] M. G. Rozman and M. Utz, Uniqueness of Reconstruction of Multiphase Morphologies from Two-Point Correlation Functions, Phys. Rev. Lett. **89**, 135501 (2002).
[20] T. Chevalier, D. Salin, L. Talon, and A. G. Yiotis, History effects on nonwetting fluid residuals during desaturation flow through disordered porous media, Phys. Rev. E **91**, 043015 (2015).
[21] J. Xu, and M. Y. Louge, Statistical mechanics of unsaturated porous media, Phys. Rev. E **92**, 062405 (2015).
[22] B. Zhao, C. W. MacMinn, and R. Juanes, Wettability control on multiphase flow in patterned microfluidics, Proc. Natl. Acad. Sci. USA **113**, 10251 (2016).
[23] S. Schlüter, S. Berg, M. Rücker, R. T. Armstrong, H.-J. Vogel, R. Hilfer, and D. Wildenschild, Pore-scale displacement mechanisms as a source of hysteresis for two-phase flow in porous media, Water Resour. Res. **52**, 2194 (2016).
[24] I. Chatzis and N. R. Morrow, Magnitude and detailed structure of residual oil saturation, SPEJ **23**, 311 (1983).
[25] R. J. Held and M. A. Celia, Pore-scale modeling extension of constitutive relationships in the range of residual saturations, Water Resour. Res. **37**, 165 (2001).
[26] V. Joekar-Niasar, F. Doster, R. T. Armstrong, D. Wildenschild, and M. A. Celia, Trapping and hysteresis in two-phase flow in porous media: A pore-network study, Water Resour. Res. **49**, 4244 (2013).

[27] C. S. Land, Calculation of imbibition relative permeability for two and three phase flow from rock properties, SPEJ **8**, 149 (1968).
[28] R. J. Lenhard and J. C. Parker, A model for hysteretic constitutive relations governing multiphase flow: 2. Permeability-saturation relations, Water Resour. Res. **23**, 2197 (1987).
[29] E. H. Spiteri, R. Juanes, M. J. Blunt, and F. M. Orr, A new model of trapping and relative permeability hysteresis for all wettability characteristics, SPEJ **13**, 277 (2008).
[30] M. Sakai, M. T. van Genuchten, A. A. Alazba, B. I. Setiawan, and B. Minasny, A complete soil hydraulic model accounting for capillary and adsorptive water retention, capillary and film conductivity, and hysteresis, Water Resour. Res. **51**, 8757 (2015).
[31] R. Hilfer, Macroscopic capillarity and hysteresis for flow in porous media, Phys. Rev. E **73**, 016307 (2006).
[32] M. L. Porter, D. Wildenschild, G. Grant, and J. I. Gerhard, Measurement and prediction of the relationship between capillary pressure, saturation, and interfacial area in a NAPL-water-glass bead system, Water Resour. Res. **46**, W08512 (2010).
[33] S. Peng and M. L. Brusseau, Air-water interfacial area and capillary pressure: Porous-medium textural effects and an empirical function, J. Hydrol. Eng. **17**, 829 (2012).
[34] V. Joekar-Niasar, M. Prodanović, M, D. Wildenschild, and S. M. Hassanizadeh, Network model investigation of interfacial area, capillary pressure and saturation relationships in granular porous media, Water Resour. Res. **46**, W06526 (2010).
[35] N. K. Karadimitriou, S. M. Hassanizadeh, V. Joekar-Niasar, and P. J. Kleingeld, Micromodel study of two-phase flow under transient conditions: Quantifying effects of specific interfacial area, Water Resour. Res. **50**, 8125 (2014).
[36] J. T. Cheng, L. J. Pyrak-Nolte, D. D. Nolte, and N. J. Giordano, Linking pressure and saturation through interfacial areas in porous media, Geophys. Res. Lett. **31**, L08502 (2004).
[37] V. Joekar-Niasar and S. M. Hassanizadeh, Specific interfacial area: The missing state variable in two-phase flow equation, Water Resour. Res. **47**, W05513 (2011).
[38] Z. Liu, A. Herring, C. Arns, S. Berg, and R. T. Armstrong, Pore-scale characterization of two-phase flow using integral geometry, Transp. Porous Media **118**, 99 (2017).
[39] R. T. Armstrong, J. E. McClure, M. A. Berrill, M. Rücker, S. Schlüter, and S. Berg, Beyond Darcy's law: The role of phase topology and ganglion dynamics for two-fluid flow, Phys. Rev. E **94**, 043113 (2016).
[40] A. L. Herring, E. J. Harper, L. Andersson, A. Sheppard, B. K. Bay, and D. Wildenschild, Effect of fluid topology on residual nonwetting phase trapping: Implications for geologic CO_2 sequestration, Adv. Water Res. **62**, 47 (2013).
[41] J. E. McClure, M. A. Berrill, W. G. Gray, and C. T. Miller, Influence of phase connectivity on the relationship among capillary pressure, fluid saturation, and interfacial area in two-fluid-phase porous medium systems, Phys. Rev. E **94**, 033102 (2016).
[42] S. Khorsandi, L. Li, and R. T. Johns, Equation of state for relative permeability, including hysteresis and wettability alteration, SPEJ **22**, 182655 (2017).
[43] H. Giesche, Mercury Porosimetry: A General (Practical) Overview, Part. Part. Sys. Char. **23**, 9 (2006).
[44] A. W. Adamson and A. P. Gast, *Physical Chemistry of Surfaces* (Wiley, Hoboken, NJ, 1997).
[45] G. F. Pinder and W. G. Gray, *Essentials of Multiphase Flow and Transport in Porous Media* (Wiley, Hoboken, NJ, 2008).
[46] C. H. Arns, M. A. Knackstedt, and K. R. Mecke, Characterisation of irregular spatial structures by parallel sets and integral geometric measures, Colloids Surfaces–Physiochem. Eng. Aspects **241**, 351 (2004).
[47] C. Scholz, F. Wirner, J. Götz, U. Rüde, G. E. Schröder-Turk, K. Mecke, and C. Bechinger, Permeability of Porous Materials Determined from the Euler Characteristic, Phys. Rev. Lett. **109**, 264504 (2012).
[48] R. Hilfer, Review on scale dependent characterization of the microstructure of porous media, Transp. Por. Media. **46**, 343 (2002).
[49] K. R. Mecke, Integral geometry in statistical physics, Int. J. Mod. Phys. B **12**, 861 (1998).
[50] J. Ohser, C. Redenbach, and K. Schladitz, Mesh free estimation of the structure model index, Image Analysis Stereol. **28**, 179 (2011).
[51] D. A. Klain, A short proof of Hadwigger's theorem, Mathematika **42**, 329 (1995).

[52] W. Nagel, J. Ohser, and K. Pischang An integral-geometric approach for the Euler-Poincaré characteristic of spatial images, J. Microscopy **198**, 54 (2000).
[53] J. Serra, *Image Analysis and Mathematical Morphology* (Academic Press, Orlando, FL, 1983).
[54] H. Hadwiger, *Vorlesungen Über Inhalt, Oberflächeund Isoperimetrie*, Lecture on Content, Surface and Isoperimetry (Springer, Berlin, 1957).
[55] H. Federer, Curvature Measures, Trans. Am. Math. Soc. **93**, 418 (1959).
[56] S. Chern, A simple intrinsic proof of the Gauss-Bonnet formula for closed Riemannian manifolds, Ann. Math. **45**, 747 (1944).
[57] W. G. Gray and C. T. Miller, Consistent thermodynamic formulations for multiscale hydrologic systems: Fluid pressures, Water Resour. Res. **43**, W09408 (2007).
[58] W. G. Gray and C. T. Miller, *Introduction to the Thermodynamically Constrained Averaging Theory for Porous Medium Systems* (Springer, Zürich, 2014).
[59] W. G. Gray and C. T. Miller, Averaging theory for description of environmental problems: What have we learned? Adv. Water Res. **51**, 123 (2013).
[60] S. Berg, H. Ott, S. A. Klapp, A. Schwing, R. Neiteler, N. Brussee, A. Makurat, L. Leu, F. Enzmann, J. Schwarz, M. Kersten, S. Irvine, and M. Stampanoni, Real-time 3D imaging of Haines jumps in porous media flow, Proc. Natl. Acad. Sci. USA **110**, 3755 (2013).
[61] A. Georgiadis, S. Berg, A. Makurat, G. Maitland, and H. Ott, Pore-scale micro-computed-tomography imaging: Nonwetting-phase cluster-size distribution during drainage and imbibition, Phys. Rev. E **88**, 033002 (2013).
[62] P. Spanne, J. F. Thovert, C. J. Jacquin, W. B. Lindquist, K. W. Jones, and P. M. Adler, Synchrotron Computed Microtomography of Porous Media: Topology and Transports, Phys. Rev. Lett. **73**, 2001 (1994).
[63] S. Schlüter, A. Sheppard, K. Brown, and D. Wildenschild, Image processing of multiphase images obtained via x-ray microtomography: A review, Water Resour. Res. **50**, 3615 (2014).
[64] J. E. McClure, Fluid Configurations in a Random Sphere Packing (2016) (dataset), doi:10.17612/P7TG68.
[65] A. Sheppard and M. Prodanovic, Network Comparison Forum (2015) (dataset), doi:10.17612/P7059V.
[66] J. E. McClure, J. F. Prins, and C. T. Miller, A novel heterogeneous algorithm to simulate multiphase flow in porous media on multicore CPU-GPU systems, Comput. Phys. Commun. **185**, 1865 (2014).
[67] M. Hilpert and C. T. Miller, Pore-morphology-based simulation of drainage in totally wetting porous media, Adv. Water Resour. **24**, 243 (2001).
[68] D. Adalsteinsson and M. Hilpert, Accurate and Efficient Implementation of pore-morphology-based drainage modeling in two-dimensional porous media, Transp. Por. Med. **65**, 337 (2006).
[69] S. Berg, M. Rücker, H. Ott, A. Georgiadis, H. van der Linde, F. Enzmann, M. Kersten, R. T. Armstrong, S. de With, J. Becker, and A. Wiegmann, Connected pathway relative permeability from pore-scale imaging of imbibition, Adv. Water Resour. **90**, 24 (2016).
[70] See Supplemental Material at http://link.aps.org/supplemental/10.1103/PhysRevFluids.3.084306 for additional details on the experiments and simulation data.
[71] J. E. McClure, M. A. Berrill, W. G. Gray, and C. T. Miller, Tracking interface and common curve dynamics for two-fluid flow in porous media, J. Fluid Mech. **796**, 211 (2016).
[72] J. E. McClure, M. A. Berrill, J. F. Prins, and C. T. Miller, Asynchronous in situ connected-components analysis for complex fluid flows, *In Situ Infrastructures for Enabling Extreme-Scale Analysis and Visualization (ISAV)* (IEEE, Salt Lake City, UT, 2016), pp. 12–17.
[73] S. N. Wood, Y. Goude, and S. Shaw, Generalized additive models for large data sets, J. Royal Stat. Soc. Ser. C **64**, 139 (2015).
[74] G. H. Golub, M. Heath, and G. Wahba, Generalized cross-validation as a method for choosing a good ridge parameter, Technometrics **21**, 215 (1979)
[75] W. G. Gray, A. L. Dye, J. E. McClure, L. J. Pyrak-Nolte, and C. T. Miller, On the dynamics and kinematics of two-fluid-phase flow in porous media, Water Resour. Res. **51**, 5365 (2015).